Detection and Monitoring of People in Collapsed Buildings Using a Rotating Radar on a UAV

Philipp Stockel, *Graduate Student Member, IEEE*, Patrick Wallrath, Reinhold Herschel, and Nils Pohl, *Senior Member, IEEE*

***Abstract*— This paper presents a UAV-driven sensor system with a rotating radar designed to locate people in collapsed buildings. A framework including motion estimation, motion compensation, tracking and clustering is proposed. The developed algorithms enable the detection of people despite the motion of the UAV. Furthermore, we propose a Bayesian target selection approach to discriminate between human targets and other objects in the environment of the UAV with high confidence. The effectiveness of the proposed algorithms is demonstrated using measurements and a vital sign reference system, showing close agreement of the respiration signal over time with an overall respiration rate accuracy of 1.3 %.**

***Index Terms*— FMCW radar, unmanned aerial vehicle (UAV), radar detection, vital signs, motion compensation.**

I. Introduction

SEARCHING for missing people in collapsed buildings is often very dangerous for the rescue workers. There are several projects working on technical alternatives [1], [2], [3]. The most common approach is the use of unmanned aerial vehicles (UAV) equipped with different sensors. The two major tasks in this application are the navigation of the drone inside the collapsed building, which is difficult because the walls block the GPS signal, and the localization of people. Within the German-Austrian project UAV-Rescue, the German side is developing a system where the UAV is equipped with a LIDAR (Light Detecting and Ranging) system for automatic indoor navigation and a rotating radar to localize people in the collapsed building [4]. This paper focuses on the latter part of localizing people with the rotating radar.

To our best knowledge, this is the first publication regarding a rotating radar on a moving platform used for indoor human presence detection. In general, there is very little research on the use of rotating radars for indoor applications as LIDAR sensors are often more suitable. But LIDAR sensors can not extract vital signs while rotating radars can if the phase of the radar signals is evaluated. Regarding the localization of humans in collapsed buildings, Bimpas et al. [5] developed a static radar system to detect people through collapsed walls. However, since it is a static radar system and the penetration depth is limited, the system has to be moved by the rescue workers which can endanger them. There are also some publications regarding radar sensors on moving platforms in indoor scenarios [6], but these do only estimate their position based on the range profiles, which is not accurate enough to compensate the motion in the phase signal. For the wider field of vital sign estimation with radars on moving platforms, Rong et al. give an overview of the current research in [7]. The approach proposed in [8] is also working with an indoor flying UAV. They use a secondary, up-looking radar sensor to compensate for the UAV motion in the data of a down-looking radar sensor. This approach only works if the UAV is hovering exactly over the person. In [9] they use a filtering approach based on the motion estimated by an IMU to remove the platform motion, which has the disadvantage that the target motion may also be removed if the target motion and the UAV motion have similar frequency components. In [10] we proposed different motion estimation and motion compensation techniques for down-looking MIMO (Multiple Input Multiple Output) radars on UAVs to enable the extraction of vital signs. While in some cases similar algorithms can be used, all current publications work in a different scenario, with different sensors or have drawbacks with respect to the considered application [11], [12], [13].

Two main problems make the detection of humans in this context difficult. First, the radar system is always moving due to the ego-motion of the UAV, which makes it impossible to distinguish between static objects and people based on motion. The second problem is that the rotating radar system has a limited rotation rate of 40 Hz. Moreover, due to the 77 GHz transmission frequency, the phase can only be unambiguously evaluated for position changes of less than 1 mm. This means that in order to detect people with the rotating radar, we need to find a way to correctly unwrap the phase signal despite the high phase ambiguity and the low frame rate.

In this paper, we propose different algorithms to estimate and compensate the motion of the radar system. This includes the estimation of rotations around the vertical axis of the radar as well as the horizontal motion of the radar system. Therefore, we also developed a new phase unwrapping algorithm that can unwrap the signal despite strong motion and high

Manuscript received 21 August 2023; revised 20 October 2023 and 5 December 2023; accepted 7 December 2023. Date of publication 13 December 2023; date of current version 21 December 2023. This work was supported by the German Federal Ministry of Education and Research under Grant 13N15549. *(Corresponding author: Philipp Stockel.)*

Philipp Stockel, Patrick Wallrath, and Nils Pohl are with the Fraunhofer Institute for High Frequency Physics and Radar Techniques, 53343 Wachtberg, Germany, and also with the Institute for Integrated Systems, Ruhr University Bochum, 44801 Bochum, Germany (e-mail: philipp.stockel@fhr.fraunhofer.de).

Reinhold Herschel is with BIT Technology Systems, 81379 Munich, Germany.

Digital Object Identifier 10.1109/TRS.2023.3342368

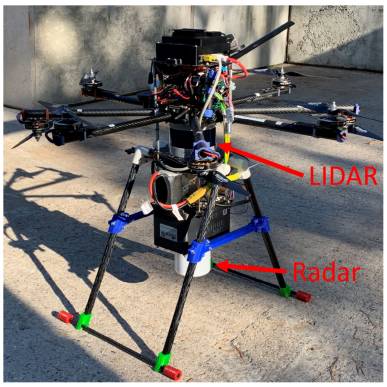

Fig. 1. Photo of the UAV equipped with rotating radar and LIDAR system.

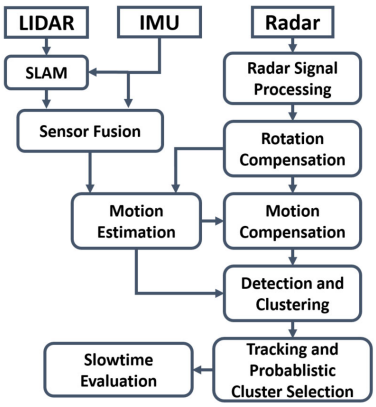

Fig. 2. Flowchart describing the overall signal processing.

phase ambiguity. We also improved the motion estimation algorithm from our previously published work [14]. Furthermore, we propose a probabilistic cluster selection approach that evaluates which tracks belong to people and which do not.

In the following, we first describe the scenario and the hardware we used. Then, we propose the framework and algorithms for motion estimation and compensation. Next, we describe how people in the environment of the radar system are detected and tracked using a probabilistic cluster selection. Finally, we present our measurement results.

II. Scenario Description

The basic scenario involves a UAV with a rotating radar and a LIDAR system mounted underneath. The UAV should automatically navigate through the collapsed buildings. Therefore, the LIDAR system provides information about the distance to all objects in the UAV's environment. The data measured by the LIDAR system, as well as the data measured by an inertial measurement unit (IMU), are fed into a SLAM (Simultaneous Localization and Mapping) algorithm to estimate the relative position of the UAV inside the building. The position estimate from the SLAM algorithm is used to navigate through the building [15]. In each new room or large area, the UAV begins to hover. While hovering, the rotating radar is used to detect people in the environment of the UAV. If a person is localized, the radar signal is evaluated to extract the chest motion and access the vital signs. Fig.1 shows an image of the UAV, equipped with the LIDAR system and the rotating radar.

III. Radar Signal Processing

The rotating radar system is a frequency modulated continuous wave (FMCW) radar transmitting at 77 GHz. The chirps scan a bandwidth of $B = 1$ GHz, resulting in a range resolution of 15 cm. The radar transmits its chirps at a repetition rate of 4 kHz. In practice, the radar itself does not rotate, but a rotating reflector reflects the signals from a static antenna onto the 360° field of view. The beam width of the radar reflector is 3° in azimuth and 1.5° in elevation. The rotation rate f_r is 40 Hz, which results in 100 chirps per rotation [16].

The distance to a target at position $\mathbf{z}$ is evaluated by calculating the Fast Fourier Transform (FFT) over the chirps. The resulting range profile for one specific direction Θ and only one target is

$$g(r,\Theta,t) = \alpha \cdot \mathrm{sinc}\left(\frac{2\pi B}{c}(r - ||\mathbf{z} - \mathbf{p}(t)||_2)\right) \cdot \exp\left(2\pi j \cdot \frac{2||\mathbf{z} - \mathbf{p}(t)||_2}{\lambda}\right) + n(t), \quad (1)$$

with r denoting the range variable, α being the amplitude of the received signal, $\mathbf{p}(t)$ the radar's position, $\lambda = \frac{c}{f_\mathrm{c}}$ the wavelength at the transmission frequency, c being the speed of light, and $n(t)$ being additive noise. The distance to the reflecting object is evaluated by finding the maximum of the sinc-term. The second term of Equation (1) includes the phase. The different range profiles are arranged according to their rotation angles. In this representation each element, called voxel in the following, has a corresponding range r and an azimuth angle Θ. Fig. 2 shows a flowchart of the entire signal processing. The individual processing steps are explained in the following chapters.

IV. Rotation Compensation

It is possible that the radar system rotates around its vertical axis while hovering. One possible way to work with the UAV rotation would be to track the targets while the UAV is rotating. However, for the considered application, long coherent detection intervals of 3 to 5 seconds are required because the human respiratory motion has a low frequency of about 0.2 Hz. If a person is located at a distance of 5 m and the UAV rotates by 30° between two detection cycles, the target would be localized at a distance of 2.6 m from the last position. This would make any tracking very difficult. Therefore, we compensate for the UAV rotation using signal processing [17].

To enable rotation compensation, the angle of rotation has to be estimated first. When the UAV starts hovering, a reference frame $g_\mathrm{ref}(r,\Theta)$, containing one chirp for every azimuth angle, is measured. This reference frame is used for comparison with each subsequent frame to estimate the relative rotation. The rotation is estimated using a cross-correlation based on the

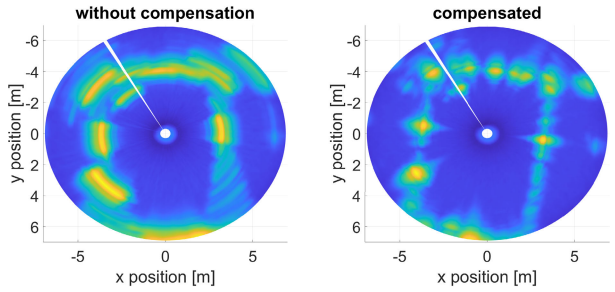

Fig. 3. Output of the detection with and without rotation compensation.

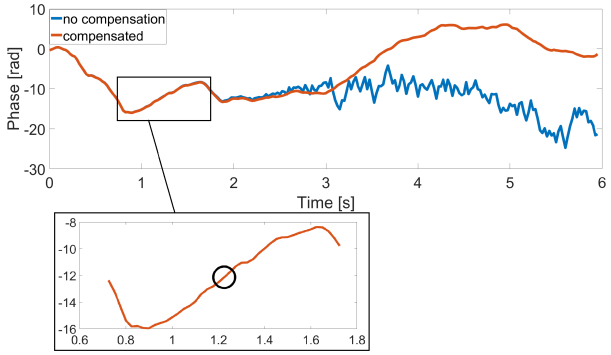

Fig. 4. Phase of a static target with and without rotation compensation. The zoomed section shows a short period around a circular shift.

Fourier transform

$$R(\Theta, t) = \mathrm{IFFT}\left\{\sum_r \left(\mathrm{FFT}\{g_{\mathrm{ref}}(r, \Theta)\} \cdot \mathrm{FFT}\{g(r, \Theta, t)\}^*\right)\right\}. \tag{2}$$

Here $(\cdot)^*$ describes the complex conjugation. In the resulting cross-correlation $R(\Theta, t)$, the rotation angle $\Theta_{\mathrm{rot}}(t)$ can be identified by finding the maximum [18], [19].

The estimated rotation angles $\Theta_{\mathrm{rot}}(\mathrm{t})$ are used to compensate for the rotation. Therefore, the frames for which the UAV is rotated relative to the reference frame have to be realigned to the reference frame. Since the data exhibits an array structure, this can be accomplished by circularly shifting the azimuth columns about

$$n_{\mathrm{rot}}(t) = \left\lfloor \frac{\Theta_{\mathrm{rot}}(t)}{\Theta_{\mathrm{res}}} \right\rceil \tag{3}$$

frames. Here $\lfloor \cdot \rceil$ is the rounding operator and Θ_{res} is the azimuth resolution. After the circular shift, the peaks in the range profiles corresponding to particular objects in the radar's environment should be located at the same azimuth angle as they would have been without a rotation of the UAV. In Fig. 3 the range-azimuth plot of a detection with and without rotation compensation is shown. Without the rotation compensation, the different peaks are spread over several azimuth angles, due to the UAV rotation. After compensation, the peaks are focused.

Another possibility would be to interpolate the radar data to the correct angles. However, this would increase the computational complexity enormously compared to the circular shift. Furthermore, due to the high azimuth resolution, there are almost no negative effects of the circular shifts on the phase of the radar signal. This can be seen if the phase of one of the static targets from Fig. 3 is analyzed. Fig. 4 shows the phase of the static target at 4.8 m distance and 220° azimuth. The blue signal was extracted before the rotation compensation, which is why after a few seconds only noise is contained. The red curve represents the signal after the rotation compensation. The signal exhibits the orthogonally projected motion of the radar system onto the direction to the static target. The zoomed area shows the sequence around a circular shift. It can be seen that there is no noticeable effect of the circular shift on the phase signal.

V. Motion Estimation

Since the movement of the UAV has to be compensated to enable the evaluation of the human chest motion, the motion of the UAV must be precisely estimated. In contrast to the position used for indoor navigation, no information about the absolute position in the room is required, but the description of position changes must be very precise.

A. Auxiliary Position

The UAV navigates through the building with the position estimation generated by the SLAM algorithm. Unfortunately, the position provided by the SLAM algorithm contains jumps caused by the limited range resolution of the LIDAR sensor and the optimization scheme of the SLAM algorithm. To remove these jumps and increase the accuracy, we use a Kalman filter to fuse the position estimate from the SLAM algorithm with the data from a second IMU integrated in the radar sensor [20], [21], [22], [23].

The accuracy of the auxiliary position is still coarsely limited by the 3 cm range resolution of the LIDAR system [24]. Since the magnitude of the breathing motion is about 1 cm, we need a more precise position estimate to compensate for the motion of the UAV. Therefore, we estimate the position based on the radar data itself and use the fused position $\mathbf{p}_{\mathrm{aux}}(t)$ as auxiliary information.

B. Wall Tracker

To get information about how the UAV's motion affects the radar signals, we can evaluate the signals reflected from static objects. This also means that we can use the reflections from different static objects in the environment of the rotating radar to get an estimate of the horizontal motion of the radar. For the considered application these objects will be the walls of the building in which the UAV is hovering.

To detect the walls, we need to measure T_{wall} seconds or $N_{\mathrm{wall}} = T_{\mathrm{wall}} \cdot f_{\mathrm{r}}$ frames of radar data. As the walls should have the highest radar cross-section (RCS) in the scene, they can be found by searching for the reflected signals with the highest average power. To find all the walls of the room, regardless of their distance to the radar, the scene is divided into N_{skip} azimuth sections. Each section contains the reflected signals $g(r, \Theta, n)$ from an interval $\Theta \in [\Theta_i, \Theta_i + \Theta_{\mathrm{skip}}]$, where Θ_i

describes the azimuth angle at which the section starts and Θ_{skip} the width of the sections. For each azimuth section the strongest reflection is located by evaluating the power, or more precisely, the average absolute value

$$M(r,\Theta) = \frac{1}{N_{\text{wall}}} \sum_{n=0}^{N_{\text{wall}}-1} |g(r,\Theta,n)| \tag{4}$$

for each signal in the section. Furthermore, we check if the reflected power from the wall is high enough with

$$20\log\left(\frac{M(r,\Theta)}{r^4}\right) > 20\log\left(\frac{M_{\max}}{r_{\max}^4}\right) - \epsilon. \tag{5}$$

Here, $M_{\max}$ and $r_{\max}$ are the range and the power of the global maximum in the scene, and ϵ is a threshold that can be chosen between 5 and 15 dB. The larger the threshold, the more walls are detected and can be used for position estimation. However, with a larger threshold it is also possible that some multipath reflections are used for position estimation. Therefore, the parameter ϵ should be chosen depending on how reverberant the expected environment is. If Equation (5) is satisfied, we identify the corresponding voxel as a wall.

If all azimuth sections have been processed, the detected walls are inserted into a tracker that tracks the walls over time and ensures that the ensemble of walls used for position estimation is as stable as possible. For every tracked wall, the movement of the radar relative to the wall is evaluated. Therefore, we calculate the phase ϕ_{wall} from the measured signal $g(r_{\text{wall}}, \Theta_{\text{wall}}, t)$ of the considered wall in direction Θ_{wall} (see Eq. (1)) using

$$\begin{aligned}\phi_{\text{wall}}(t) &= \angle g(r_{\text{wall}}, \Theta_{\text{wall}}, t) \\ &= \tan^{-1}\left(\frac{\text{Im}\{g(r_{\text{wall}}, \Theta_{\text{wall}}, t)\}}{\text{Re}\{g(r_{\text{wall}}, \Theta_{\text{wall}}, t)\}}\right).\end{aligned} \tag{6}$$

Then, we need to unwrap the phase signal over time. Unfortunately, classical unwrapping algorithms will not reconstruct the true motion because the UAV's position can change about 10 mm between consecutive samples, while classical unwrapping only works for changes smaller than $\frac{\lambda}{4} = 0.97$ mm. This problem arises mainly due to the low frame rate, which can not be increased because the rotation rate is already at its mechanical limit [25], [26].

To overcome this problem, we proposed an assisted unwrapping algorithm that uses position data from other sensors to assist the unwrapping process in [14]. Unfortunately, this method requires a quite accurate auxiliary position. More precisely, if we project the auxiliary position onto the direction of some target and calculate the differences between successive samples, the error compared to using the true position must be less than $\frac{\lambda}{4}$. Due to the limited resolution of the LIDAR system and the geometric distance between the center of the UAV and the center of the radar, the auxiliary position described in Section V-A does not reach the required position accuracy. Therefore, we propose a new unwrapping algorithm, shown in Algorithm 1, which is capable of working with stronger motions and higher phase ambiguity.

In this algorithm, the lines 1 through 7 are similar to a classical unwrapping algorithm. So $\phi[k]$ at line 7 describes

Algorithm 1 Second Derivative Unwrapping

input : wrapped phase signal $\phi[k]$
length K of signal $\phi[k]$ with $k = 1, \ldots, K$
output: unwrapped phase signal $\phi[k]$

1 $\tilde{\rho} = 0$, $\rho = 0$, $\tilde{\phi} = 0$, $\tilde{\mathrm{d}\phi} = 0$
2 **for** $(k = 2; k <= K; k = k + 1)$ **do**
3 $\quad \mathrm{d}\phi = \tilde{\rho} \cdot 2\pi + \phi[k] - \tilde{\phi}$
4 $\quad$ **if** $d\phi > \pi$ **then**
5 $\quad\quad \tilde{\rho} = \tilde{\rho} - 1$
6 $\quad$ **else if** $d\phi < -\pi$ **then**
7 $\quad\quad \tilde{\rho} = \tilde{\rho} + 1$
8 $\quad \phi[k] = \phi[k] + \tilde{\rho} \cdot 2\pi$
9 $\quad \mathrm{d}\phi = \phi[k] - \tilde{\phi}$
10 $\quad \tilde{\phi} = \phi[k]$
11 $\quad \mathrm{d}^2\phi = \mathrm{d}\phi - \tilde{\mathrm{d}\phi}$
12 $\quad \tilde{\mathrm{d}\phi} = \mathrm{d}\phi$
13 $\quad$ **if** $d^2\phi > \pi$ **then**
14 $\quad\quad \delta = -1$
15 $\quad$ **else if** $d\phi < -\pi$ **then**
16 $\quad\quad \delta = 1$
17 $\quad$ **else**
18 $\quad\quad \delta = 0$
19 $\quad \sigma = \sigma + \delta$
20 $\quad \rho = \rho + \sigma$
21 $\quad \phi[k] = \phi[k] + \rho \cdot 2\pi$
22 **end**

an incorrectly unwrapped signal. The incorrect unwrapping results in a sudden change in the slope, or more precisely, in the first derivative of the phase signal. A jump in the first derivative can be detected by calculating the second derivative and checking for peaks, as done in the lines 8 through 17. If there is a negative peak, then the first derivative contains a negative jump. This means that we have to add 2π to the first derivative of the incorrectly unwrapped phase signal to remove the jump. Consequently, 2π have to be subtracted if there is a positive peak. The correctly unwrapped signal can then be calculated by integrating the corrected first derivative. The proposed Algorithm 1 uses the integer values δ, σ and ρ to describe how many times we have to add or subtract 2π to get the correct second derivative, first derivative and unwrapped signal, respectively. In reality, the algorithm is not implemented as a for-loop, but is called with each new phase value for each wall tracked. Fig. 5 shows the results of the proposed unwrapping for a simulated signal

$$\phi_{\text{sim}}(t) = 125 \cdot (\cos(2\pi t \cdot 0.5) - 1) \tag{7}$$

$$\phi'_{\text{sim}}(t) = \angle \exp(j\phi_{\text{sim}}(t)), \tag{8}$$

with $\phi'_{\text{sim}}(t)$ being the wrapped phase signal.

The red line describes the phase signal $\phi(t)$ unwrapped using the classical unwrapping algorithm, which is also the intermediate result from line 7 of Algorithm 1. The yellow line describes how many full cycles have to be added to $\phi(t)$ to get a correctly unwrapped signal. Finally, the purple line shows the result of the Second Derivative Unwrapping. As it is exactly aligned with the green dots, which correspond to the

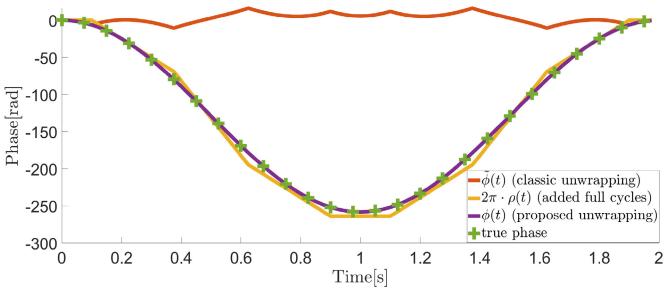

Fig. 5. Unwrapped phase of a simulated signal using the proposed unwrapping algorithm (purple), together with the true phase (green), the results using a classical unwrapping algorithm (red) and a signal describing the number of full cycles which were added to correctly unwrap the signal (yellow).

true unwrapped phase $\phi_{\text{sim}}(t)$, we can argue that the proposed algorithm can unwrap the signal correctly while the classical unwrapping can not.

The algorithm has two weak points. First, if a new wall is detected, an easy way to initialize the integer variable for the first derivative σ would be to set it to 0. However, if at that moment the true first derivative of the phase is greater than 2π, the unwrapped phase is incorrect. Therefore, we need to estimate σ during initialization. The auxiliary position $\mathbf{p}_{\text{aux}}[k]$ can be used to calculate an estimation of the phase signal

$$\phi_{\text{aux}}[k] = \frac{4\pi}{\lambda} \cdot \begin{pmatrix} \cos(\Theta_{\text{wall}}) \\ \sin(\Theta_{\text{wall}}) \\ 0 \end{pmatrix} \cdot \mathbf{p}_{\text{aux}}[k]^{\text{T}}. \tag{9}$$

This allows the calculation of an estimate of the first derivative $\text{d}\phi_{\text{aux}}$, which can then be used to calculate the approximate number of full cycles with which σ has to be initialized. The second weakness occurs if a peak in the second derivative is missed or incorrectly recognized. This leads to incorrect values of the integer variable for the first derivative σ, which then implies that the unwrapped phase signal differs more and more from the true unwrapped phase with each new sample. To overcome this, the unwrapped phase $\phi[k]$ is compared to $\phi_{\text{aux}}[k]$. If the difference is bigger than the threshold $30 \cdot 2\pi$, the unwrapping algorithm will be reset.

To validate the benefits of the proposed unwrapping algorithm, we show in Fig. 6 the results for a measured phase signal and a projected motion of about 15 cm. The red line describes the phase signal $\phi(t)$ unwrapped using the classical unwrapping algorithm. The yellow line again describes how many full cycles have to be added to $\phi(t)$ to get a correctly unwrapped signal. Finally, the purple line shows the result of the Second Derivative Unwrapping. In blue, we have also plotted the phase signal without any unwrapping. To allow a better comparison between the proposed unwrapping, the classic unwrapping and the wrapped phase signal, we also show a zoomed view of the first three seconds.

C. Motion Calculation

Before estimating the position, the mechanical rotation of the radar has to be compensated. Since the radar rotates at a rate f_{r}, the signals for the different angles Θ are measured over a period of $T_{\text{r}} = 1/f_{\text{r}}$ seconds. For an accurate position

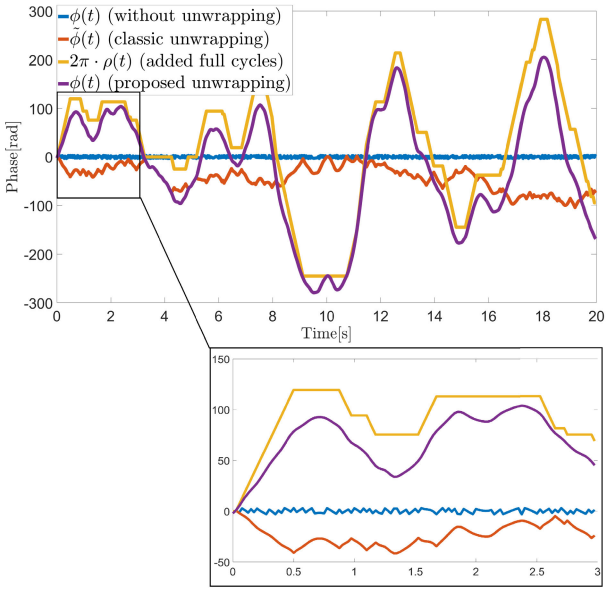

Fig. 6. Unwrapped phase using the proposed unwrapping algorithm (purple), together with the signal without any unwrapping (blue), the results using a classical unwrapping algorithm (red) and a signal describing the number of full cycles which were added to correctly unwrap the signal (yellow).

estimation, the time shift between the different measurements has to be compensated by interpolating the measured phase signals $\phi[k]$ for each wall with

$$\phi[k] = \phi[k] - (\phi[k] - \phi[k-1]) \cdot \frac{\Theta - 2\pi}{2\pi}. \tag{10}$$

Afterwards, the movements measured at the different angles of the rotation are aligned with each other. This means that we can use the phase signals of the detected walls to estimate the position. However, the position estimation is only accurate if the ensemble of detected walls is well distributed. For example, if only two walls have been detected and their angles Θ differ by 180°, a precise position estimation is not possible because there is no information about the motion perpendicular to the axis between the two detected walls. Therefore, we check if for at least two of all detected walls the absolute angular difference

$$\alpha = |\Theta_1 - \Theta_2| \% 180 \tag{11}$$

will be greater than 30°. Here, % is the modulo operator and Θ_1 and Θ_2 are the azimuth angles of the two walls.

If the ensemble of M detected walls is valid, the current position of the radar system and the UAV can be estimated by solving a localization problem. The basic idea is that the unwrapped phase signals are the orthogonal projection of the motion, and therefore the motion can be computed by evaluating the projection from the different walls with a system of equations. We build the equation system

$$A\mathbf{p} = \mathbf{y} \quad \text{with}$$
$$A = \begin{pmatrix} -\cos(\Theta_1) & -\sin(\Theta_1) \\ \vdots & \vdots \\ -\cos(\Theta_M) & -\sin(\Theta_M) \end{pmatrix},$$

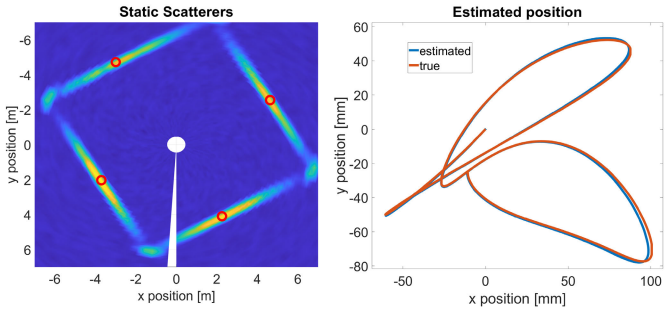

Fig. 7. Simulated scenario with four walls. The static targets used for position estimation are marked in the detector output on the left side. On the right side the estimated position is shown together with the true position of the radar.

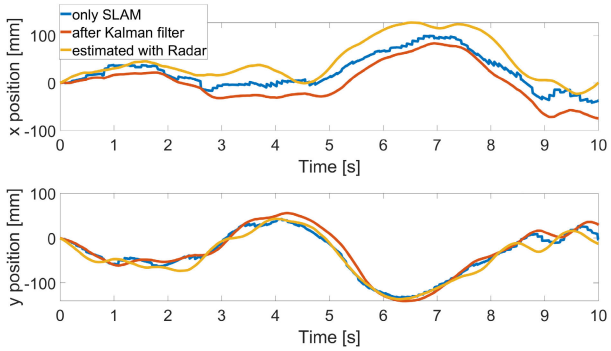

Fig. 8. Position estimation in x- and y-direction over time for the SLAM algorithm (blue), the Kalman filtered combination of SLAM and IMU (red) and the radar based motion estimation (yellow).

$$\mathbf{y} = \frac{\lambda}{4\pi}\begin{pmatrix}\phi_1(t)\\ \vdots \\ \phi_M(t)\end{pmatrix} \tag{12}$$

using the azimuth angles $\Theta_1, \Theta_2, \ldots, \Theta_M$ and the unwrapped phase values $\phi_1, \phi_2, \ldots, \phi_M$ of the detected walls. The equation system can be solved e.g. by the method of least squares, and the solution corresponds to the current position of the UAV

$$\mathbf{p} = \begin{pmatrix}x\\ y\end{pmatrix}. \tag{13}$$

The position estimation is performed for each new radar frame, resulting in the estimation of the radar motion $\mathbf{p}(t)$. Note that $\mathbf{p}(t)$ is only a relative and not an absolute motion estimation because it only describes the change in position relative to the moment in which the wall tracking has started.

To evaluate the accuracy of the position estimation, a simulated scenario is used. On the left side of Fig. 7 the detected static scatterers used for position estimation are marked. On the right side of Fig. 7 the estimated position for 10 seconds of simulated measurement data is shown together with the true position. Over the whole measurement time, the differences between the true and estimated positions are very small and the overall root mean square error (RMSE) is 0.94 mm. Fig. 8 shows the results for a measured dataset. It can be seen that the position estimate of the SLAM algorithm and the auxiliary position calculated by fusing the SLAM position with the data of an IMU using a Kalman filter are coarsely aligned with the position estimated using the radar data. However, comparing the proposed position estimate with the SLAM position, there is an RMS error of 4.7 cm and even comparing with the auxiliary position, the RMS error is still at 3.9 cm. Thus, the auxiliary position can not be used for motion compensation and we have to estimate the position with the proposed approach [14].

VI. Localization of Human Targets

A. Motion Compensation

To compensate the motion of the radar system, we have to calculate the compensation signal for every direction Θ. Therefore, the estimated motion $\mathbf{p}(t)$ is projected onto the directions Θ with

$$\phi_{\text{proj}}(t) = \frac{4\pi}{\lambda} \cdot \begin{pmatrix}\cos(\Theta)\\ \sin(\Theta)\end{pmatrix} \cdot \mathbf{p}(t)^{\text{T}}. \tag{14}$$

Again, we have to take into account the mechanical rotation. Therefore, the projected phase signals are interpolated with

$$\phi_{\text{proj}}(t) = \phi_{\text{proj}}(t) + (\phi_{\text{proj}}(t) - \phi_{\text{proj}}(t - T_{\text{r}})) \cdot \frac{\Theta - 2\pi}{2\pi} \tag{15}$$

so that they are exactly aligned with the measurement time for the angle Θ. Here, T_{r} is the duration of one rotation. Comparing the equations (10) and (15), we see that (15) reverses the interpolation from (10). The projected and interpolated phase signals are then used to compensate the motion for all the angles Θ with

$$g_{\text{comp}}(r, \Theta_{\text{meas}}, t) = g(r, \Theta_{\text{meas}}, t) \cdot \exp(-j \cdot \phi_{\text{proj}}(t)). \tag{16}$$

Since the compensation signal depends only on the azimuth angle, the same compensation signal $\phi_{\text{proj}}(t)$ can be used for all range bins in the corresponding direction Θ [10], [27], [28].

B. Detection and Clustering

After motion compensation, people in the scene can be localized. The detection is performed blockwise every T_{det} seconds on $N_{\text{det}} = T_{\text{det}} \cdot f_{\text{r}}$ radar frames. To detect the people in the scene, we use an FFT to compute the Doppler representation $G(r, \Theta, f)$ on the detection interval for each voxel. The Doppler describes the relative velocity of the objects reflecting the radar signals. As the respiratory motion has a magnitude of 5 to 20 mm and a frequency of about 0.2 Hz, we can expect motions with a velocity v between $v_{\text{min}} = 1\ \frac{\text{mm}}{\text{s}}$ and $v_{\text{max}} = 4\ \frac{\text{mm}}{\text{s}}$. Using

$$f_{\text{Doppler}} = \frac{2 \cdot v}{\lambda} \tag{17}$$

we can calculate the frequency boundaries $f_{\text{min}} \approx 0.5$ Hz and $f_{\text{max}} \approx 2$ Hz, between which respiratory motion should be present. Therefore, the detector

$$D(r, \Theta) = \sum_{f_{\text{min}} < f < f_{\text{max}}} |G(r, \Theta, f)| \tag{18}$$

should contain high values for breathing humans [29].

The voxels for which

$$20\log(D(r, \Theta)) > 20\log(D_{\text{max}}) - 40\ \text{dB}, \tag{19}$$

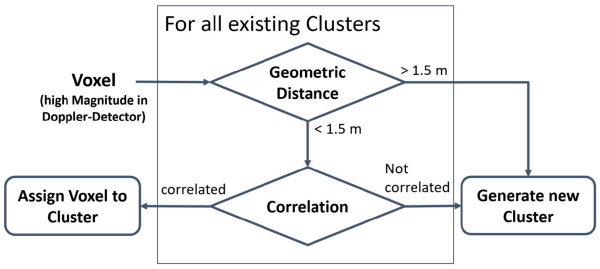

Fig. 9. Flowchart describing the clustering algorithm.

with $D_{\max}$ being the maximum of the Doppler detector, are sorted in descending order by their magnitude and inserted into the clustering algorithm. Each selected voxel (r_i, Θ_i), with $i = 1, .., I$ and the number of strong voxels I, has its specific cartesian position $\mathbf{p}_i$ and a corresponding slowtime signal $s_i(t)$. Since the detection block is executed every T_{det} seconds, the slowtime signals contain N_{det} values. For each selected voxel, we first check if there is already an existing cluster geometrically close to the new voxel by checking the euclidean distance

$$||\mathbf{p}_i - \mathbf{p}_k||_2 < 1.5, \text{ m} \quad k = 1, \ldots, K. \tag{20}$$

Here, $\mathbf{p}_k$ with $k = 1, \ldots, K$ are the cartesian positions of the existing clusters, with K as the number of existing clusters. If the new voxel does not belong to any of the existing clusters, a new cluster is created with the new voxel as its center. If the new voxel is geometrically close to an existing cluster, we check if the slowtime signals of the voxel and the cluster contain similar features. Therefore, we calculate the central value of the cross-correlation between the slowtime signal of the voxel $s_i(t)$ and the slowtime signal of the cluster $s_k(t)$ with

$$R_{s_i s_k}(0) = \frac{1}{N_{\text{det}}} \sum_{n=0}^{N_{\text{det}}-1} s_i(n) \cdot s_k(n)^*. \tag{21}$$

If

$$\frac{R_{s_i s_k}(0)}{\sqrt{R_{s_k s_k}(0) \cdot R_{s_i s_i}(0)}} > 0.7, \tag{22}$$

the new voxel is assigned to the cluster. Otherwise, a new cluster is generated. If the left side of Equation (22) is 1, the signals are identical. The threshold value of 0.7 was chosen based on heuristics. In Equation (21), $s(n)^*$ is the complex conjugate of $s(n)$ and $R_{s_i s_i}(0)$ and $R_{s_k s_k}(0)$ are the central values of the auto-correlation of s_i and s_k, respectively. Fig. 9 shows a flowchart of the clustering process.

The K detected clusters are then fed into a tracking algorithm. For each cluster, we check if there is already a tracked cluster from the previous detection cycles with a similar geometric position by examining

$$||\mathbf{p}_k - \mathbf{p}_m||_2 < 1.5, \quad m = 1, \ldots, M. \tag{23}$$

Here, $\mathbf{p}_k$ with $k = 1, \ldots, K$ are the center positions of the clusters detected in the current detection cycle and $\mathbf{p}_m$, with $m = 1, \ldots, M$ being the center positions of the already tracked clusters. If the euclidean distance is less than 1.5 m, the cluster is assigned to the track and the center position as well as the slowtime signal are updated with the data of the new cluster. A cluster that is not assigned to any of the existing tracked clusters, will be added to the tracker as a new track as long as the maximum number of tracks is not reached. If two or more clusters would be assigned to an existing track, only the closest cluster will be assigned to it, while the other clusters will be inserted as new tracks if the maximum number of tracks has not yet been reached. If a tracked cluster is not updated for more than two consecutive detection cycles, the track is deleted.

C. Probabilistic Cluster Selection

Unfortunately, the motion compensation can never completely remove the motion of the UAV. For example, there is always a small error between the true azimuth angle from which a signal was reflected and the azimuth angle of the voxel where the reflected signal was detected. Therefore, the orthogonally projected compensation signal is also slightly off, resulting in a residual motion. This residual motion is most of the time smaller than the motion of the target, but since the RCS of walls is much higher than the RCS of people, there might still be some large peaks corresponding to walls in the Doppler detector. This leads to tracked clusters, which do not correspond to a person. Since we only want to detect and monitor people, we use a Probabilistic Cluster Selection (PCS), which should ensure that only people and not walls or other static objects in the scene are tracked [30].

PCS is based on the calculation of a probability that describes the likelihood that a cluster corresponds to a person. The probability is built from four base probabilities:

- **Geometric probability** P_{geo}, it is unlikely that a person is distributed over an area larger than 0.5 m,
- **Motion probability** P_{mot}, the phase should not be the residual of the compensated UAV motion,
- **Respiration probability** P_{resp}, the amplitude of the phase should be in the range of typical values for the respiration,
- **RCS probability** P_{rcs}, the radar cross-section of a person should be at a certain level.

The geometric probability P_{geo} utilizes that the chest motion of a person should be restricted to an area smaller than 0.5 meters. Walls or other static objects often occupy an area much larger than that. We use this property to define the probability as

$$P_{\text{geo}} = \begin{cases} \gamma_{\text{geo}} & d_{\max} \leq 0.5 \text{ m} \\ 1 - \gamma_{\text{geo}} & d_{\max} > 0.5 \text{ m} \end{cases}, \tag{24}$$

with $d_{\max}$ being the maximum distance between two elements in the cluster and $0 < \gamma_{\text{geo}} < 1$ being a parameter that defines how large the influence of the geometric probability should be. In our experiments, $\gamma_{\text{geo}} = 0.75$ gave good results. Since all clusters that occupy a big area should have a geometric probability smaller than 0.5, the total probability for these clusters should also be relatively small.

The motion probability P_{mot} examines the similarity of the phase to the UAV motion. Therefore, we evaluate if the phase signal and the UAV motion $\mathbf{p}(t)$ are linear dependent, by solving the equation

$$A\mathbf{x} = \mathbf{b} \tag{25}$$

with $\mathbf{b} = \frac{\lambda}{4\pi}\phi(t)$ as the unwrapped phase of the target in the current detection cycle and $A = \mathbf{p}(t)^{\mathrm{T}}$ as a $N_{\mathrm{det}} \times 2$ matrix containing the UAV motion. By solving the equation system using least squares, we obtain $\mathbf{x}$ as the factors of the linear combination closest to $\mathbf{b}$. By analyzing the relative residual

$$v_{\mathrm{res}} = \frac{1}{N_{\mathrm{det}}} \sum_{n=0}^{N_{\mathrm{det}}-1} |\mathbf{b} - A\mathbf{x}|, \tag{26}$$

we can assess to which degree the phase signal is resulting from the imperfect compensation of the UAV motion. The residual v_{res} is then used to calculate the residual probability with

$$P_{\mathrm{mot}} = \begin{cases} \gamma_{\mathrm{mot}} & v_{\mathrm{res}} \geq 5 \text{ mm} \\ 1 - \gamma_{\mathrm{mot}} & v_{\mathrm{res}} < 5 \text{ mm} \end{cases}. \tag{27}$$

The threshold value of 5 mm was chosen based on heuristics and $0 < \gamma_{\mathrm{mot}} < 1$ is again a parameter defining the influence of the probability, which was set to 0.75 in our experiments. The residual probability discards all clusters whose phase signal is influenced only by the remaining UAV motion.

The third base probability evaluates the resemblance of the unwrapped phase signals with a respiratory motion. The amplitude of the respiratory motion is typically about 1 cm. Therefore, all clusters for which the unwrapped phase of the slowtime signal has a amplitude much larger or much smaller are unlikely to correspond to a person. The amplitude a for a cluster's phase signal is calculated with

$$a = \xi_{\mathrm{resp}} \cdot \frac{\lambda}{4\pi}(\max\{\phi(t)\} - \min\{\phi(t)\}), \tag{28}$$

with $\phi(t)$ being the unwrapped phase signal from the central cluster voxel for the detection interval and $\min\{\cdot\}$ and $\max\{\cdot\}$ being operators which take the minimum and maximum value of a signal, respectively. The factor $\xi_{\mathrm{resp}} = 100$ is used to scale the amplitude in a way that the probability distribution has the desired properties. Using a, we can compute the probability P_{mag} with

$$P_{\mathrm{resp}} = \frac{1}{\sqrt{2\pi\sigma_{\mathrm{resp}}^2}} \exp\left(\frac{-(a - \mu_{\mathrm{resp}})^2}{2\sigma_{\mathrm{resp}}^2}\right). \tag{29}$$

Here, the parameters $\mu_{\mathrm{resp}} = \xi_{\mathrm{resp}} \cdot 7$ mm and $\sigma_{\mathrm{resp}} = \xi_{\mathrm{resp}} \cdot 4$ mm are chosen based on the typical amplitude of the respiration and the deviation of likely amplitude values. We estimated both parameters based on multiple radar measurements with different people in different orientations.

The last base probability is based on the reflected power in the specific voxel and the distance to it. Therefore, the reflected power in the current detection interval is scaled by the corresponding distance with

$$S = \frac{1}{r^4} \frac{1}{N_{\mathrm{det}}} \sum_{n=0}^{N_{\mathrm{det}}-1} |s(n)|. \tag{30}$$

The normalized reflected power is then used to calculate the probability

$$P_{\mathrm{rcs}} = \frac{1}{\sqrt{2\pi(\xi_{\mathrm{rcs}} \cdot \sigma_{\mathrm{rcs}})^2}} \exp\left(\frac{-(\xi_{\mathrm{rcs}} S - \xi_{\mathrm{rcs}}\mu_{\mathrm{rcs}})^2}{2(\xi_{\mathrm{rcs}} \cdot \sigma_{\mathrm{rcs}})^2}\right), \tag{31}$$

which describes how likely it is that a target with a specific radar cross-section, in this case represented by the normalized reflected power, corresponds to a person. The parameters μ_{rcs} and σ_{rcs} are estimated by analyzing the normalized reflected power for people at different distances and poses. Both parameters are highly dependent on the radar system and have to be scaled with a factor ξ_{rcs}. The scaling parameter ξ_{rcs} is defined by

$$\xi_{\mathrm{rcs}} = \frac{\sigma_{\mathrm{rcs}}}{0.2} \tag{32}$$

and should again ensure that the probability density function has the desired properties.

The four base probabilities are then combined to the likelihood

$$P(d_j|\text{is person}) = \min(P_{\mathrm{geo}}, P_{\mathrm{mot}}) \cdot \frac{P_{\mathrm{resp}} + P_{\mathrm{rcs}}}{2}, \tag{33}$$

which represents the probability that the data of a cluster in the j^{th} detection cycle corresponds to a person. The operator $\min(a, b)$ takes the smaller one of the two input arguments. This operator is chosen because the influence of a multiplicative combination of the two base probabilities P_{geo} and P_{mot} on the combined probability would be too strong.

Afterwards, Bayes' theorem is used to compute the posterior probability

$$P(\text{is person}|d_j) = \frac{P(d_j|\text{is person}) \cdot P(\text{is person})}{P(d_j)}, \tag{34}$$

describing the probability that the hypothesis is correct based on the data measured in the j^{th} detection cycle. Here is

$$\begin{aligned} P(d_j) = {} & P(d_j|\text{is person}) \cdot P(\text{is person}) \\ & + P(d_j|\text{not person}) \cdot P(\text{not person}), \end{aligned} \tag{35}$$

with $P(\text{is person})$ and $P(\text{not person})$ being the prior probabilities for the hypothesis. Since most of the detected targets do not correspond to humans, we initialized the priors with $P(\text{not person}) = 0.8$ and $P(\text{is person}) = 0.2$ [31].

The probabilities for the tracked clusters are updated in each detection step. Thus, the posterior from the last detection cycle is used as the prior for the next detection cycle. This means that P_{j-1}^m is the prior of the hypothesis *is person* for the m^{th} tracked cluster in the j^{th} detection cycle. Since there are only two cases, the prior of the hypothesis *not person* for the m^{th} tracked cluster in the j^{th} detection cycle is described with $(1 - P_{j-1}^m)$. Furthermore, we define the likelihood that the m^{th} cluster's data in the j^{th} detection cycle corresponds to a person with $\tilde{P}_j^m$. This results in the following Bayesian update

$$P_j^m = \frac{\tilde{P}_j^m \cdot P_{j-1}^m}{\tilde{P}_j^m \cdot P_{j-1}^m + (1 - \tilde{P}_j^m) \cdot (1 - P_{j-1}^m)}. \tag{36}$$

Because of this iterative probability update, the prediction of whether a tracked cluster belongs to a person or a static object becomes more reliable with each iteration. This allows to remove tracks which have a probability of less than 10 % to belong to a person over multiple detection cycles. After hovering for 20 seconds, only clusters belonging to people should be tracked. By evaluating the corresponding slowtime signals, the vital signs of these people can be estimated [31], [32], [33].

Fig. 10. Photo of measurement with a person and the UAV equipped with rotating radar and LIDAR at TCRH in Mosbach.

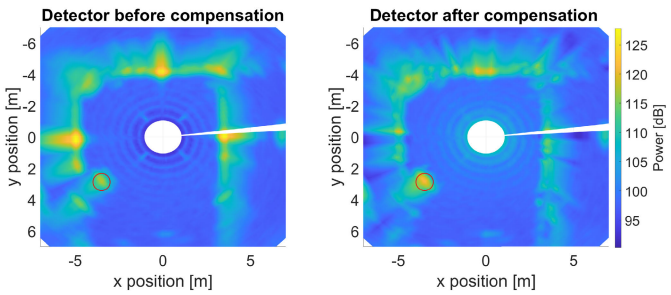

Fig. 11. Detector output before and after motion compensation.

VII. Results

To test the proposed algorithms, a measurement campaign was carried out at the TCRH in Mosbach, Germany. The UAV, equipped with LIDAR-System and rotating radar, flew in a room with a person[1] sitting on a chair. The scenario is shown in Fig. 10. To verify the measurements the person was connected to a vital sign reference system [34].

Processing begins with the detection of the walls or other static objects with high RCS in the environment of the radar system. For each wall detected, the phase signals are extracted, unwrapped using Algorithm 1, and used to estimate the precise radar position. Then, the position estimate is used to compensate for the UAV's motion in the radar data. By analyzing the motion contained in the phase signal reflected from static objects before and after the compensation for different measurements we can see that the motion is reduced from about 200 mm to less than 4 mm. This means that we can compensate for about 98 % of the motion.

After compensating for the UAV's motion, the people in the environment of the radar can be detected. Fig. 11 shows the results of the detection algorithm from Equation (18) before and after the motion compensation. The position of the person is marked in both plots. It can be seen that before the compensation the peak corresponding to the person is much weaker than the peaks corresponding to the walls. After compensation, the peak corresponding to the person is the largest.

[1]Informed consent was obtained from all subjects.

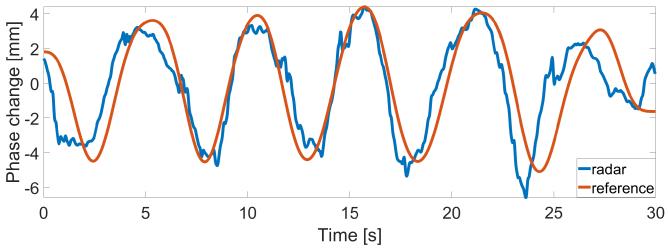

Fig. 12. Depiction of the phase signal extracted from a detected person together with the respiration motion measured by the reference system.

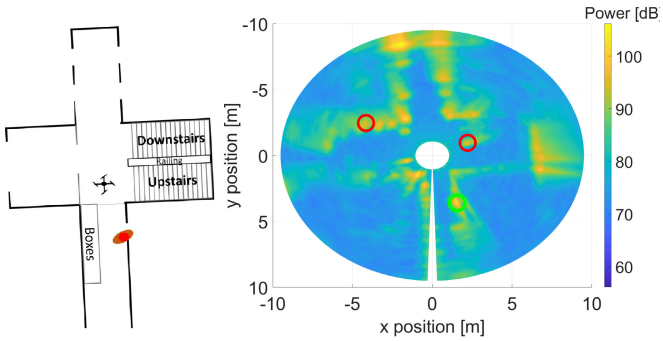

Fig. 13. Detector output for a reverbant environment with a schematic of the environment on the left side and markers for the targets chosen with the probablistic cluster selection.

If a person is detected, we can extract the slowtime signal and calculate the unwrapped phase signal. Fig. 12 shows the unwrapped phase signal extracted from the target belonging to the person. For comparison, we have also plotted the respiratory motion measured by the vital sign reference system. The similarities are easy to see. If we compare the respiration rate predicted from the unwrapped phase signal $\hat{f}_{\text{resp}} = 11.13$ bpm with the respiration rate measured by the reference system $f_{\text{resp}} = 10.99$ bpm, we get a relative error of 1.33 %.

Unfortunately, in more complicated or reverberant environments, the peaks corresponding to people are often weaker than some of the static targets, even after motion compensation. This can be caused by large movements of the radar, multipath reflections, small motion of the person, or unwrapping problems in the apparent detection cycles. Therefore, we have to track different detected targets over time and estimate how likely it is that the tracks belong to a person by using the Probabilistic Cluster Selection. Fig. 13 shows the detector output for such a reverberant environment. For a better understanding of the scenario, we also give a graphical description of the environment, showing the position of the person in the scene. The three marked scatterers in the detector output correspond to two false targets (red) and the person (green).

Using the Probabilistic Cluster Selection, many of the strong scatterers can be removed immediately because they are initialized with a probability of belonging to a person smaller than 0.1, while some of the targets with similar RCS as a human will also have higher probabilities of belonging to a person. However, due to the Bayesian probability update, these targets can also be removed after some detection cycles, leaving only

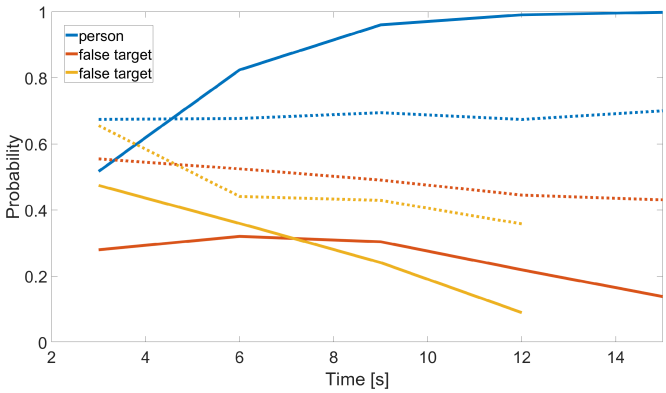

Fig. 14. Bayesian probability development for different targets. The dotted lines represent the accompanying a-priori probabilities for the different tracks.

those targets that correspond most likely to a human. Fig. 14 shows the estimated probability for the three marked scatterers from Fig. 13. Here, the dotted lines represent the calculated probability that the target belongs to a person based on the data measured in the current detection cycle, while the solid lines represent the posterior probabilities after the Bayesian update. It can be seen that the posterior probabilities for the targets belonging to walls tend to zero, while the posterior probability of the target belonging to the person becomes more confident with each iteration. This means that we can use the Probabilistic Cluster Selection to remove all targets that do not belong to a person.

VIII. Conclusion

In this research, algorithmic solutions were developed to locate missing people in collapsed buildings using a rotating radar mounted underneath a UAV. This involved estimating the UAV's rotations around its vertical axis and estimating the UAV's horizontal motion using the reflected radar signals of different static targets in the environment of the radar system. A new unwrapping algorithm was proposed to enable the motion estimation based on the reflected signals. Using the motion estimates, the rotation and the motion of the UAV were compensated in the radar data. After the motion compensation, more than 98 % of the UAV's motion are removed from the radar signals. In the compensated radar data, the human targets in the environment of the UAV can be detected, clustered and tracked using a Bayesian approach that distinguishes human targets from other objects. Finally, we have demonstrated the effectiveness of the proposed algorithms by localizing people in the environment of the UAV in a realistic scenario. Furthermore, we have extracted their chest motion and verified the measured respiration rate with a vital sign reference system, showing high signal overlap in the time domain as well as an overall respiration rate error of only 1.33 %.

References

[1] A. K. M. Z. Islam, D. Hanna, and A. Ferworn, "Volunteer drone: Search and rescue of the industrial building collapsed worker," in *Proc. 4th Int. Conf. Wireless, Intell. Distrib. Environ. Commun.*, I. Woungang and S. K. Dhurandher, Eds. Cham, Switzerland: Springer, 2022, pp. 99–110.

[2] J. Dong, K. Ota, and M. Dong, "UAV-based real-time survivor detection system in post-disaster search and rescue operations," *IEEE J. Miniaturization Air Space Syst.*, vol. 2, no. 4, pp. 209–219, Dec. 2021.

[3] INACHUS *The INACHUS Project*, Courtesy of the American Concrete Institute, Farmington Hills, MI, USA, 2018, pp. 19–21.

[4] R. Herschel et al. (2022). *UAV-Borne Remote Sensing for AI-Assisted Support of Search and Rescue Missions*. [Online]. Available: https://publica.fraunhofer.de/handle/publica/440397

[5] M. Bimpas, N. Paraskevopoulos, K. Nikellis, D. Economou, and N. K. Uzunoglu, "Development of a three band radar system for detecing trapped alive humans under building ruins," *Prog. Electromagn. Res.*, vol. 49, pp. 161–188, 2004. [Online]. Available: https://api.semanticscholar.org/CorpusID:55136390

[6] A. Safa et al., "FMCW radar sensing for indoor drones using variational auto-encoders," in *Proc. IEEE Radar Conf.*, May 2023, pp. 1–6.

[7] Y. Rong, R. Gutierrez, K. V. Mishra, and D. W. Bliss, "Noncontact vital sign detection with UAV-borne radars: An overview of recent advances," *IEEE Veh. Technol. Mag.*, vol. 16, no. 3, pp. 118–128, Sep. 2021.

[8] R. H. Nakata, B. Haruna, T. Yamaguchi, V. M. Lubecke, S. Takayama, and K. Takaba, "Motion compensation for an unmanned aerial vehicle remote radar life sensor," *IEEE J. Emerg. Sel. Topics Circuits Syst.*, vol. 8, no. 2, pp. 329–337, Jun. 2018.

[9] N. Poole, S. Hor, and A. Arbabian, "A real-time, frame-level platform vibration compensation approach for mmWave radar systems," in *Proc. 18th Eur. Radar Conf. (EuRAD)*, Apr. 2022, pp. 181–184.

[10] P. Stockel, P. Wallrath, R. Herschel, and N. Pohl, "Motion compensation in six degrees of freedom for a MIMO radar mounted on a hovering UAV," *IEEE Trans. Aerosp. Electron. Syst.*, vol. 59, no. 5, pp. 5791–5801, Oct. 2023, doi: 10.1109/TAES.2023.3266181.

[11] R. Nakata, S. Clemens, A. Lee, and V. Lubecke, "RF techniques for motion compensation of an unmanned aerial vehicle for remote radar life sensing," in *IEEE MTT-S Int. Microw. Symp. Dig.*, May 2016, pp. 1–4.

[12] Y. Rong, A. Herschfelt, J. Holtom, and D. W. Bliss, "Cardiac and respiratory sensing from a hovering UAV radar platform," in *Proc. IEEE Stat. Signal Process. Workshop (SSP)*, Jul. 2021, pp. 541–545.

[13] S. M. M. Islam, C. Grado, V. Lubecke, and L. C. Lubecke, "UAV radar sensing of respiratory variations for COVID-type disorders," in *Proc. IEEE Asia–Pacific Microw. Conf. (APMC)*, Dec. 2020, pp. 737–739.

[14] P. Stockel, P. Wallrath, N. Pohl, and R. Herschel, "High accuracy position calculation of a hovering UAV using a rotating radar," in *Proc. 19th Eur. Radar Conf. (EuRAD)*, Sep. 2022, pp. 129–132.

[15] J. Rotter and B. Wagner, "Calibration of a 2D scanning radar and a 3D LiDAR," in *Proc. 19th Int. Conf. Informat. Control, Autom. Robot.*, 2022, pp. 377–384.

[16] Indurad GmbH. (Apr. 2023). *iSDR—Radar Sensor*. [Online]. Available: https://www.indurad.com/technology/sensors/isdr/

[17] J. Yu, A. Dewantari, and M.-H. Ka, "Measurement of the rotation center from the received signals for ultrahigh-resolution radar imaging," *IEEE Antennas Wireless Propag. Lett.*, vol. 16, pp. 2266–2269, Jun. 2017.

[18] L. Zheng, Y. Wang, and C. Hao, "Cross-correlation registration algorithm based on the image rotation and projection," in *Proc. 4th Int. Congr. Image Signal Process.*, vol. 2, Oct. 2011, pp. 1095–1098.

[19] M. B. Hisham, S. N. Yaakob, R. A. A. Raof, A. B. A. Nazren, and N. M. Wafi, "Template matching using sum of squared difference and normalized cross correlation," in *Proc. IEEE Student Conf. Res. Develop. (SCOReD)*, Dec. 2015, pp. 100–104.

[20] P. Stockel, P. Wallrath, R. Herschel, and N. Pohl, "Correlation-based motion estimation for the compensation of horizontal movements of a hovering UAV," in *Proc. 17th Eur. Conf. Antennas Propag. (EuCAP)*, Mar. 2023, pp. 1–5.

[21] P. Wallrath and R. Herschel, "MIMO radar based platform motion detection for radar imaging," in *Proc. 21st Int. Radar Symp. (IRS)*, Oct. 2020, pp. 351–355.

[22] B. Li, L. Yang, J. Xiao, R. Valde, M. Wrenn, and J. Leflar, "Collaborative mapping and autonomous parking for multi-story parking garage," *IEEE Trans. Intell. Transp. Syst.*, vol. 19, no. 5, pp. 1629–1639, May 2018.

[23] W. Hess, D. Kohler, H. Rapp, and D. Andor, "Real-time loop closure in 2D LiDAR SLAM," in *Proc. IEEE Int. Conf. Robot. Autom. (ICRA)*, May 2016, pp. 1271–1278.

[24] I. V. Lidar. (Apr. 2023). *Puck LITE*. [Online]. Available: https://velodynelidar.com/products/puck-lite/#downloads

[25] Y. Chen, F. Wang, J.-W. Wan, G. Li, and K. Xu, "An ambiguity-reduced phase unwrapping method and its applications in parameter estimation," in *Proc. IEEE Int. Conf. Signal Process., Commun. Comput. (ICSPCC)*, Sep. 2015, pp. 1–4.

[26] N. Han, Z. Fan, and S. Fang, "Phase unwrapping methods for solving the ambiguity in current velocity estimation based on combined signal design," *Flow Meas. Instrum.*, vol. 59, pp. 126–134, Mar. 2018. [Online]. Available: https://www.sciencedirect.com/science/article/pii/S0955598617302601

[27] R. Sharma, "A clutter based motion estimation and compensation technique for a nonstationary radar platform," in *Proc. IEEE Conf. Radar*, Jan. 2006, pp. 1–4.

[28] S. M. M. Islam, L. C. Lubecke, C. Grado, and V. M. Lubecke, "An adaptive filter technique for platform motion compensation in unmanned aerial vehicle based remote life sensing radar," in *Proc. 50th Eur. Microw. Conf. (EuMC)*, Jan. 2021, pp. 937–940.

[29] S. M. M. Islam, L. Oba, and V. M. Lubecke, "Empirical mode decomposition (EMD) for platform motion compensation in remote life sensing radar," in *Proc. IEEE Radio Wireless Symp. (RWS)*, Jan. 2022, pp. 41–44.

[30] Z. Xie, B. Zhou, X. Cheng, E. Schoenfeld, and F. Ye, "Passive and context-aware in-home vital signs monitoring using co-located UWB-depth sensor fusion," *ACM Trans. Comput. Healthcare*, vol. 3, no. 4, pp. 1–31, Nov. 2022, doi: 10.1145/3549941.

[31] J. Mochnac, S. Marchevsky, and P. Kocan, "Bayesian filtering techniques: Kalman and extended Kalman filter basics," in *Proc. 19th Int. Conf. Radioelektronika*, Apr. 2009, pp. 119–122.

[32] M. S. Arulampalam, S. Maskell, N. Gordon, and T. Clapp, "A tutorial on particle filters for online nonlinear/non-Gaussian Bayesian tracking," *IEEE Trans. Signal Process.*, vol. 50, no. 2, pp. 174–188, Feb. 2002.

[33] D. Reid, "An algorithm for tracking multiple targets," *IEEE Trans. Autom. Control*, vol. AC-24, no. 6, pp. 843–854, Dec. 1979.

[34] *HealthLab Satelliten-Maste SAT-0M*, Koralewski Industrie-Elektronik HG, Hambühren, Germany, Aug. 2015.

Philipp Stockel (Graduate Student Member, IEEE) received the B.Sc. degree in telecommunication engineering and the M.Sc. degree in electrical engineering from the University of Applied Science in Münster, Germany, in 2018 and 2020, respectively. He is currently pursuing the Ph.D. degree with Ruhr University Bochum, Germany. Then, he was a Researcher with the University of Applied Science in Münster, for nine months, before moving to the Fraunhofer Institute for High Frequency Physics and Radar Techniques, Wachtberg, Germany, where he is a Researcher. His research interests include radar signal processing, with focus on detection and tracking, motion compensation, and vital sign estimation.

Patrick Wallrath received the M.Sc. degree in electrical engineering from the University of Applied Sciences Trier in 2020. Since 2020, he has been a Researcher with the Fraunhofer Institute for High Frequency Physics and Radar Techniques FHR. Since 2022, he has been leading a team working on 3D sensor systems with Fraunhofer FHR. His main research interests are development and optimization of MIMO radar signal processing algorithms for detection, tracking, motion analysis, and human vital parameter estimation.

Reinhold Herschel received the Dipl.-Ing. degree from the Dresden University of Technology, Dresden, Germany, in 2008, and the degree from Helmut Schmidt University, Hamburg, Germany, in 2014. In 2008, he was a Ph.D. Student with the Communications Laboratory, Dresden University of Technology. He joined the Fraunhofer Institute for High Frequency Physics and Radar Techniques FHR, Wachtberg, Germany, where he led a team focusing on radar signal and image processing for integrated radar sensors until 2022. He currently builds up the Radar Signal Processing and Simulation Group, BIT Technology Solutions, Dresden.

Nils Pohl (Senior Member, IEEE) received the Dipl.-Ing. and Dr.-Ing. degrees in electrical engineering from Ruhr University Bochum, Bochum, Germany, in 2005 and 2010, respectively. From 2006 to 2011, he was a Research Assistant with Ruhr University Bochum, where he was involved in integrated circuits for millimeter-wave (mm-wave) radar applications. In 2011, he became an Assistant Professor with Ruhr University Bochum. In 2013, he became the Head of the Department of mm-wave Radar and High Frequency Sensors, Fraunhofer FHR, Wachtberg, Germany. In 2016, he became a Full Professor of integrated systems with Ruhr University Bochum. In parallel, he is the Head of the Research Group for Integrated Radar Sensors, Fraunhofer FHR. He has authored or coauthored more than 200 scientific papers and has issued several patents. His current research interests include ultra-wideband mm-wave radar, design, and optimization of mm-wave integrated SiGe circuits and system concepts with frequencies up to 500 GHz and above; and frequency synthesis and antennas. He is a member of VDE, ITG, EUMA, and URSI. He was a co-recipient of the 2009 EEEfCom Innovation Award. He was a recipient of the Karl-Arnold Award of the North Rhine-Westphalian Academy of Sciences, Humanities and the Arts in 2013; and the IEEE MTT Outstanding Young Engineer Award in 2018. Additionally, he was a co-recipient of the Best Paper Award at EUMIC 2012; the Best Demo Award at RWW 2015; and the Best Student Paper Awards at RadarConf 2020, RWW 2021, and EUMIC 2021.